NANO LETTERS

2001
Vol. 1, No. 7
383−386

Synthesis of Silicon Nanocrystals with Erbium-Rich Surface Layers

Robert A. Senter, Yandong Chen, and Jeffery L. Coffer*

Department of Chemistry, Texas Christian University, Ft. Worth, Texas 76129

Leandro R. Tessler*

Instituto de Física "Gleb Wataghin", Universidade Estadual de Campinas, 13083−970 Campinas, SP, Brazil

Received April 30, 2001; *Revised Manuscript Received June 18, 2001*

ABSTRACT

A route to silicon nanocrystals with erbium-rich surface layers is described involving the initial pyrolysis of disilane to produce nucleation and growth of the Si core followed by a second thermal annealing step in the presence of the volatile complex Er(tmhd)$_3$ (tmhd = 2,2,6,6-tetramethyl-3,5-heptanedionato). These nanoparticles were structurally characterized by transmission electron microscopy, selected area electron diffraction, energy-dispersive X-ray analysis, and extended X-ray absorption fine structure methods, while spectroscopic characterization was achieved via photoluminescence and UV–visible absorption spectroscopies. The effects of altering the length of the pyrolysis oven and its temperature, the disilane flow rate, and the Er(tmhd)$_3$/helium carrier gas flow rate on the mean nanoparticle feature size are noted. Interestingly, the characteristic Er^{3+} near-infrared photoluminescence at 1540 nm is not detected in the as-formed nanoparticles but can be observed after a brief vacuum anneal at 800 °C.

The ability of silicon to act as a viable optoelectronic platform in future applications depends strongly on legitimate routes to overcome its intrinsic inability to emit light.[1] At present, the formation of luminescent nanophase Si[2,3] and rare earth incorporation into single-crystal Si[4−7] are being extensively studied as potential solutions to this dilemma. For the latter approach, the rare earth ion erbium is of particular interest because its $^4I_{13/2} \rightarrow {}^4I_{15/2}$ luminescent transition at 1.54 μm lies at a transmission maximum for silica-based waveguides.[4−8] Such studies have mainly involved erbium implanted into bulk Si[8] or porous Si,[9] the codeposition of erbium and silicon thin films, both crystalline[10] or amorphous[11] spin-on films,[12] or erbium deposited into Si nanocrystal-rich SiO_2.[13] Recently, a process utilizing the kinetic trapping of erbium ions during the nucleation and growth of silicon nanoparticles in the gas phase has been developed in our laboratories.[14] Importantly, these doped nanocrystals retain the desired luminescence at 1540 nm associated with the erbium centers. However, as a consequence of the synthetic method and the fact that erbium centers can diffuse easily at the growth temperature of the pyrolysis oven (∼1000 °C),[15] a relatively random dispersion of dopant site environments within the nanocrystal is anticipated. Thus, routes to a more directed control of Er^{3+} location warrant attention for both fundamental and applied perspectives, as spatial distribution of erbium centers should impact the recombination of carriers generated either electrically or with light. This letter details our preparation of silicon nanocrystals with erbium-rich surfaces; such a process involves the initial pyrolysis of disilane to produce nucleation and growth of the Si core, followed by a second thermal annealing step in the presence of the volatile complex Er(tmhd)$_3$ (tmhd = 2,2,6,6-tetramethyl-3,5-heptanedionato). These initial experiments have focused on the effects of varying the length of the pyrolysis oven and its temperature, the disilane flow rate, and the Er(tmhd)$_3$/helium carrier gas flow rate on the mean nanoparticle feature size. Details of the local erbium coordination environment and the spectroscopic properties of the nanocrystals are described as well.

Experimental Section. *Nanoparticle Synthesis.* The reactor, based on a modification of an original design by Littau et al. for the synthesis of homogeneous Si nanocrystals,[16] is constructed from 7 mm inner diameter quartz tubing, with gas flow regulated by mass-flow controllers (MKS Inc.). Diluted disilane in He (0.48% Si_2H_6 (Praxair)) travels at selected rates (see Table 1) through a small pyrolysis oven (either 3 or 6 cm in length) operating at 1000 °C. After pyrolysis the aerosol is mixed with Er(tmhd)$_3$ vapor (Strem) in He carrier gas (Praxair, UHP grade) and approximately 4 cm from the introduction of the erbium precursor the aerosol is again heated at temperatures ranging from 750 to 900 °C with a small oven. After the second pyrolysis step, the reaction mixture travels downstream to a dual bubbler system where the aerosol is collected as an ethylene glycol colloid.

* To whom correspondence should be addressed. E-mail: j.coffer@tcu.edu.

10.1021/nl015546d CCC: $20.00
Published on Web 07/11/2001

Scheme 1

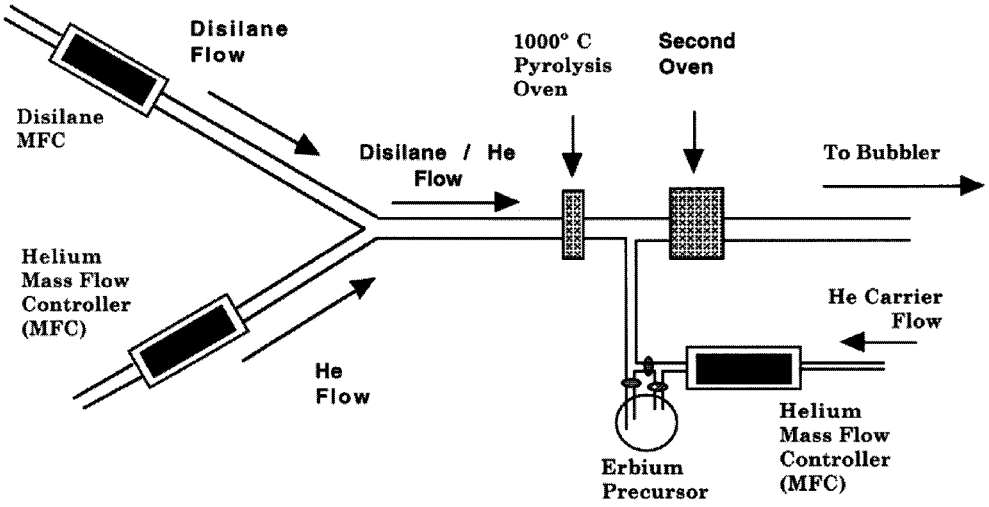

Table 1. Impact of Flow Rates, Oven Temperatures, and Lengths on the Average Diameter of Erbium-Doped Nanoparticles[a]

flow rates (sccm)			oven temp (°C)		oven lengths (cm)			
He (disilane)	He (Er)	diluted disilane	first	second	first	second	av size (nm)	std dev (nm)
3000	1500	3.1	1000	750	3	6.5	22.5	7.2
3000	2000	5.8	1000	750	3	6.5	26.2	7.7
3000	1500	3.3	1000	900	3	6.5	26.2	9.7
3000	2000	3.3	1000	750	3	6.5	20.7	4.7
3000	1500	3.3	1000	750	6	6.5	26.7	8.5
3000	NA	3.1	1000	NA	3	NA	13.8	4.8
3000	NA	3.1	1000	NA	6	NA	15.2	6.6

[a] The first five rows correspond to data for the Si nanocrystals with erbium-rich surface layers, while the last two rows list the size information for Si nanocrystals with erbium in a random distribution of site environments.

At the end of a 24 h reaction period, the reaction mixture consists of a yellow colloid and brown solid. After initial separation by centrifugation, the supernatant is treated with THF in a ratio of 10:1 (THF:ethylene glycol) to force precipitation of a solid product. The product is washed several times with ethanol to remove physisorbed erbium ions. For characterization purposes, this precipitate can be redissolved in ethylene glycol.

Instrumentation. Structural characterization of Er^{3+}-doped Si nanocrystals was performed using a JEOL 200CX TEM at the University of North Texas. Samples were deposited on carbon films on copper grids, and ethylene glycol was allowed to evaporate prior to imaging. X-ray energy dispersive spectroscopy (XEDS) analyses of Er^{3+}-doped aggregates were performed in the scanning transmission electron microscopy (STEM) mode of the JEOL 200CX. Selected area electron diffraction patterns (SADP) were obtained during TEM analyses. UV−visible spectra were obtained using a Hewlett-Packard 8452A diode array spectrometer. Low-resolution (±4 nm) near-IR photoluminescence (PL) spectra were obtained using an Applied detector Corp. liquid N_2-cooled Ge detector in conjunction with a Stanford Research Systems Chopper/Lock-in amplifier and an Acton Research Corp. 0.25 m monochromator. Excitation was provided by a Coherent Ar^+ laser operating at 488 nm and 450 mW power. A 10 cm lens was used to focus light from the sample onto the monochromator entrance slit. Emitted light was collected at 45° angle relative to the excitation direction. A 1000 nm cutoff filter (Melles Griot) was positioned over the monochromator entrance slit to filter out second- and third-order light.

Extended X-ray absorption spectroscopy (EXAFS) at the Er L3 edge was performed at the XAS beamline of the Brazilian National Synchrotron Light Laboratory (LNLS) storage ring at Campinas, SP, Brazil. X-ray absorption was measured by fluorescence with a N_2-cooled Canberra SL30165 Si(Li) detector and standard photon counting techniques with the samples kept at room temperature. Since the Er concentration in the samples is small, long acquisition times (several hours) were necessary to obtain reasonable signal-to-noise ratios. Samples of bulk Er_2O_3 and a thin film of $ErSi_2$ were used as reference standards for determining coordination numbers and bond lengths.

Results and Discussion. To direct the Er^{3+} centers in a narrower spatial location for a given nanocrystallite, the pyrolysis reactor design was altered from our original design[14] to decouple the initial nucleation and growth steps of the silicon nanocrystals from the erbium incorporation step (Scheme 1). The initial pyrolysis of dilute disilane results in the nucleation and growth of kinetically trapped Si nanocrystals; the second pyrolysis oven achieves decomposition of the $Er(tmhd)_3$ precursor followed by growth of the shell.

A conventional bright-field transmission electron micrograph of a sample prepared under the conditions associated with the 20.7 nm sample (Table 1) is shown in Figure 1. Numerous high-contrast particles of nanometer dimension are clearly observed. The selected area electron diffraction patterns (SADP) of these nanocrystals (Figure 2a), clearly consistent with the diamond-cubic phase of silicon, exhibit discrete, intense spots rather than the broadened ring patterns in the case of Er^{3+} centers randomly dispersed in the crystalline Si host.[14] While some sharpness in the diffraction

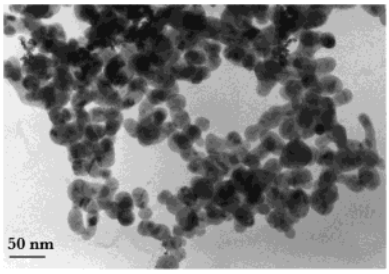

Figure 1. Conventional bright-field transmission electron micrograph of a Si nanocrystal sample with an erbium-rich surface, prepared under the conditions associated with the 20.7 nm sample given in Table 1.

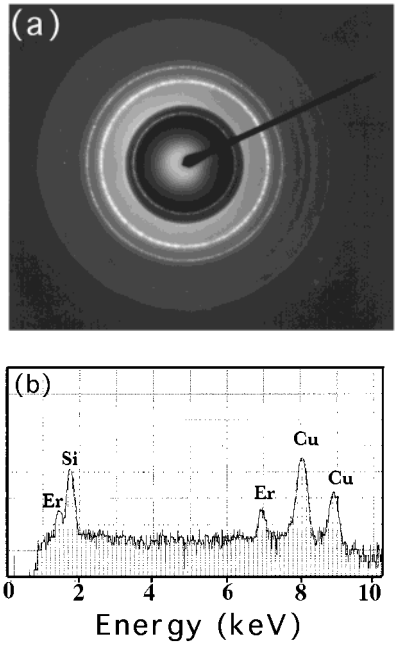

Figure 2. (a) Selected area electron diffraction pattern for the 20.7 nm average size sample illustrated in Figure 1. (b) X-ray energy dispersive spectrum from a dark contrast area in part (a).

pattern is expected as a consequence of larger particle size, such observations are consistent with the erbium present on the shell of the nanocrystal. It is also important to note that there is no evidence of elemental Er, Er silicide, or Er oxide phases in these diffraction patterns.

X-ray energy dispersive spectroscopy (XEDS) analysis of these doped nanocrystals was performed in the scanning transmission electron microscopy (STEM) mode (Figure 2b). As expected, the spectra indicate the presence of Si, and importantly, the Er-L and Er-M peaks at 6.9 and 1.4 keV, respectively. When compared to previously reported data for randomly dispersed Er dopants in silicon nanocrystals,[14] a lower limit for the erbium concentration of 2% can be estimated for the samples measured here. Similar SADP and XEDS results were found for samples generated under the different parameters listed in Table 1.

For all of the nanocrystal samples obtained under the experimental conditions noted in Table 1, the average structure size was determined by measuring 200−600 individual structure diameters for each type. The average

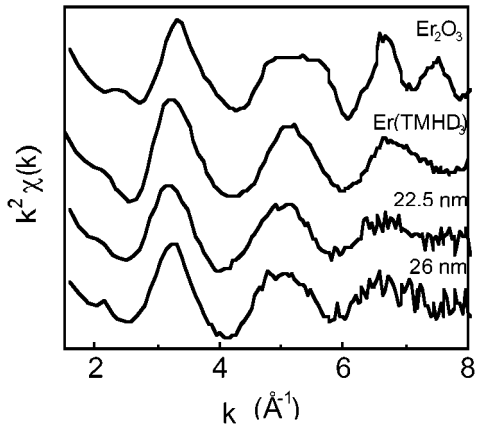

Figure 3. Erbium EXAFS signals for the Si samples with 26 and 22.5 nm average particle size, as well as for the Er(tmhd)$_3$ precursor and the standard compound Er_2O_3.

diameter and associated standard deviations are presented in Table 1. In the sequential layered growth approach employed here, the presence of the erbium results in a slightly larger nanocrystal on average, as expected. This is in stark contrast to the originally reported Er^{3+} randomly dispersed nanocrystals, where the presence of the Er^{3+} centers during Si nanoparticle nucleation and growth catalyzed the formation of smaller Si nanostructures.[17] Such discriminating observations are clearly consistent with the proposed Er-rich shell structure.

For those nanocrystals containing surface-enriched erbium, the effects of increasing pyrolysis oven length, disilane flow rate, and second oven temperature exhibit very subtle increases in terms of average structure size, albeit within a standard deviation. Such subtleties are reasonable: a longer oven time permits a longer nucleation and growth period of the Si embryo structures; a higher disilane flow obviously increases the Si concentration per unit time in the reactor; a higher operating temperature in the second oven results in more efficient shell growth under the conditions evaluated. However, increasing the carrier gas flow rate associated with the erbium precursor results in a very slight decrease in feature size, presumably a consequence of shorter residence time for the nanocrystal in the second oven.

Figure 3 represents the EXAFS signals for samples with 26 and 22.5 nm average particle size, as well as for the precursor and the standard compound Er_2O_3. The relative phase of the oscillations indicate that Er is coordinated to oxygen in the nanoparticles. To determine the coordination N, Er−O atomic separation r, and the Debye−Waller factor σ^2, we fitted the k^2 weighted EXAFS function for the filtered first neighbor peak using phases and amplitudes obtained from the Er_2O_3 standard. Both nanoparticle samples have similar Er neighborhoods. We obtained $N = 6.6 \pm 0.7$, $r = 2.30 \pm 0.01$ Å, and $\sigma^2 = 0.001 \pm 0.001$ Å^2 for a 26 nm sample and $N = 6.9 \pm 0.7$, $r = 2.31 \pm 0.01$ Å, and $\sigma^2 = 0.003 \pm 0.001$ Å^2 for a 22.5 nm sample. These parameters indicate an Er_2O_3-like environment, reminiscent of the oxygen octahedra that constitute the Er first coordination shell in Er(tmhd)$_3$. The Er−O bond lengths are markedly greater than those of Er_2O_3 ($r = 2.26$ Å). This structure is

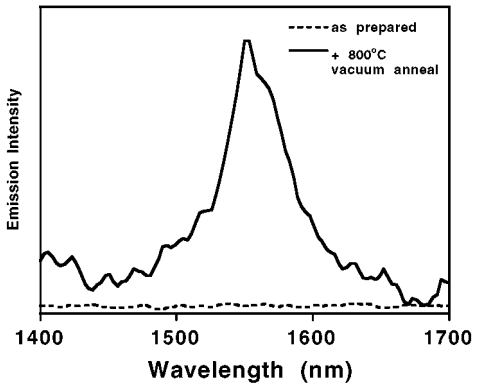

Figure 4. Room-temperature photoluminescence spectra of a 20.7 nm Si nanocrystal sample with an erbium-rich surface, illustrating the effects of an 800 °C anneal on the near-IR emission associated with the Er^{3+} centers. An excitation wavelength of 488 nm at a power of 450 mW was utilized for the spectra shown.

also in stark contrast to the Er−O coordination environment of randomly dispersed Er^{3+}-doped Si nanocrystals with less than 3 nm average particle size[18] where the coordination number is lower and the Er−O distance on average is shorter. Clearly, the different growth mechanism of the nanoparticles containing Er-rich surface layers manifests itself in a different local erbium environment. In these samples the Er sites are not constrained by the Si lattice, allowing a less constrained Er_2O_3-like Er environment. The longer bond lengths are interpreted as a consequence of the fact that virtually all the Er is located in the first atomic layers of the nanoparticle surface. The Er−O interaction energy is reduced by surface relaxation, and consequently, the interatomic separation increases.

The as-formed Si nanocrystals possessing Er-rich surface layers, with a coordination number near 6, do not demonstrate the 1540 nm luminescence associated with the Er^{3+} centers. The randomly dispersed Er^{3+}-doped Si nanocrystals with lower oxygen coordination, however, do emit at this wavelength at room temperature.[14] The evolution of the Er neighborhood with annealing in Er implanted crystalline Si shows that strong Er luminescence is associated with Er being coordinated to oxygen, in a local symmetry breaking configuration.[19] Clearly, the reason for the lack of photoluminescence in our samples is something else. We can speculate that the local Er concentration in the outer atomic shells is so high that the photoluminescence is quenched by Er−Er cross relaxation.

Preliminary thermal annealing experiments of the Si nanocrystals with Er-rich surfaces find that a brief 800 °C vacuum treatment results in strong near-IR photoluminescence at 1540 nm in this material (Figure 4). Although the structural impact of this anneal is yet to be elucidated, it should be noted that at such high temperatures Er−O complexes can diffuse in Si, increasing the Er−Er separation and thus rapidly decreasing the cross relaxation probability.

Summary. In general, this type of synthetic approach provides a complementary contrast to our previously reported approach to rare earth incorporation into Si nanoparticles, which yielded a range of rare earth structural environments within the Si host (i.e., both surface and interior sites). The approach described here, in principle useful for a variety of other dopants, yields relatively more control of the dopant atom(s) location in the Si nanocluster structure. Further experiments analyzing the effect of altering shell structure and composition on the nanocrystal photophysics are in progress.

Acknowledgment. We gratefully acknowledge the National Science Foundation (DMR-9819178), the Robert A. Welch Foundation, CNPq, and FAPESP for financial support of this research. Partial support was also provided by LNLS-National Synchrotron Light Laboratory, Brazil. Experimental assistance in the EXAFS measurements from Dr. M. C. Martins Alves is also acknowledged.

References

(1) Iyer, S.; Xie, Y.-H. *Science* **1993**, *260*, 40.
(2) Canham, L. *Appl. Phys. Lett.* **1990**, *57*, 1046.
(3) For a recent review of porous silicon, see: Stewart. M.; Buriak, J. *Adv. Mater*. **2000**, *12*, 860.
(4) Ennen, H.; Schneider, J.; Pomrenke, G.; Axmann, A. *Appl. Phys. Lett*. **1983**, *90*, 943.
(5) Ennen, H.; Pomrenke, G.; Axmann, A.; Eisele, K.; Haydl, W.; Schneider *J. Appl. Phys. Lett*. **1985**, *46*, 381.
(6) Benton, J. L.; Michel, J.; Kimerling, L. C.; Jacobson, D. C.; Xie, Y.-H.; Eaglesham, D. J.; Fitzgerald, E. A.; Poate, J. M. *J. Appl. Phys*. **1991**, *70*, 2667.
(7) Adler, D. L.; Jacobsen, D. C.; Eaglesham, D. J.; Marcus, M. A.; Benton, J. L.; Poate, J. M.; Citrin, P. H. *Appl. Phys. Lett*. **1992**, *61*, 2181.
(8) Polman, A. *J. Appl. Phys*. **1997**, *82*, 1.
(9) (a) Namavar, F.; Lu, F.; Perry, C. H.; Cremins, A.; Kalkhoran, N.; Soref, R. *J. Appl. Phys*. **1995**, *77*, 4813. (b) Hömmerich, U.; Namavar, F.; Cremins, A.; Bray, K. *Appl. Phys. Lett*. **1996**, *68*, 1951. (c) Tsybeskov, L.; Duttagupta, S.; Hirschman, K.; Fauchet, P.; Moore, K.; Hall, D. *Appl. Phys. Lett*. **1997**, *70*, 1790. (d) Lopez, H. A.; Fauchet, P. M. *Appl. Phys. Lett*. **1999**, *75*, 3989. (e) Lopez, H. A.; Fauchet, P. M. *Appl. Phys. Lett*. **2000**, *77*, 3704.
(10) Thilderkvist, A.; Michel, J.; Ngiam, S.; Kimerling, L.; Kolenbrander, K. *Mater. Res. Soc. Symp. Proc*. **1995**, *405*, 265.
(11) For a review of amorphous silicon, see: Tessler, L. R. *Braz. J. Phys*. **1999**, *29*, 616. Tessler, L. R.; Iñiguez, A. C. In *Amorphous and Microcrystalline Silicon Technology − 1998*; Wagner, S., Hack, M., Branz, H. M., Schroope, R., Shimizu, I., Eds.; Materials Research Society Proceedings 507; MRS: Pittsburgh, 1998; pp 505−517.
(12) Dorofeev, A.; Gaponenko, N.; Bondarenko. V.; Bachilo, E.; Kazuchits, N.; Leshok, A.; Troyanova, Vorosov, N. Borisenko, V.; Gnaser, H.; Bock, H.; Becker, P.; Oechsner, H. *J. Appl. Phys*. **1995**, *77*, 2679.
(13) (a) Kik, P. G.; Polman, A. *J. Appl. Phys*. **2000,** *88*, 1992. (b) Franzo, G.; Pacifici, D.; Vinviguerra, V.; Priolo, F.; Iacona, F. *Appl. Phys. Lett*. **2000**, *76*, 2167. (c) Kenyon, A. J.; Chryssou, C.; Pitt; C. W. *Appl. Phys. Lett*. **2000**, *76*, 688.
(14) St. John, J.; Coffer, J. L.; Chen, Y.; Pinizzotto, R. F. *J. Am. Chem. Soc*. **1999**, *121*, 1888.
(15) Polman, A.; Custer, J.; Zagwijn, P.; Molenbroek, A.; Alkemade, P. *J. Appl. Phys.* **1997**, *81*, 150.
(16) Littau, K.; Szajowski, P.; Muller, A.; Kortan, A.; Brus, L. *J. Phys. Chem*. **1993**, *97*, 1224.
(17) St. John, J.; Coffer, J. L.; Chen, Y.; Pinizzotto, R. F. *Appl. Phys. Lett*. **2000**, *77*, 1635.
(18) Tessler, L. R.; Coffer, J. L.; Ji, J.; Senter, R. To be published.
(19) Terrasi, A.; Franz, G.; Coffa, S.; Priolo, F.; 'Acapito, F. D.; Mobilio, S. *Appl. Phys. Lett*. **1997**, *70*, 1712.

NL015546D